

Molecular Dynamics Simulations of Bulk Native Crystalline and Amorphous Structures of Cellulose

K. Mazeau* and L. Heux

CERMAV-CNRS, Université J. Fourier, BP 53, 30841 Grenoble Cedex 9, France

Received: August 22, 2002; In Final Form: November 25, 2002

Molecular modeling has been performed on three cellulosic systems: the two native crystalline phases ($I\alpha$ and $I\beta$) and an amorphous phase, constituted by four independent microstructures. The goal of the study is to describe different organizations of the material and to emphasize how crystalline and amorphous celluloses differ. Besides, the study of the crystal structures for which many experimental data are available allows an estimation of the ability of the force field to model condensed phases of cellulose. For these organized structures the bulk parameters, such as unit cell dimensions, densities, Hildebrand solubility parameters, and hydrogen bonding, compare favorably well with the available experimental measures. The individual cellulose chains conformational behavior is as expected: torsion angles of the glycosidic bonds explore the g -values, hydroxymethyl groups are in the tg orientation, and the pyranoid ring puckering is in the 4C_1 chair form. On the contrary, all the conformational parameters of the amorphous models show large variations: preferred values of the glycosidic bond torsion angles reproduce, however, the potential energy surface of cellobiose model compound. Furthermore, the Φ torsion angle behavior is in good concordance with the exo-anomeric effect. Hydroxymethyl groups explore mostly the gg and gt orientations, and high-energy puckering of the pyran rings is stabilized within the amorphous solid. Interchain interactions on both amorphous and crystalline structures are analyzed by means of the hydrogen bonding network. Finally, estimation of the glass transition temperature of an amorphous microstructure is given.

1. Introduction

Cellulose is the most abundant renewable organic substance on earth. An essential component of various natural composites such as wood, it is one of the most popular and the most used polysaccharide by industry in either its native or regenerated forms. Material mechanical properties strongly depend on the ratio between crystalline and amorphous phases; crystalline cellulose has such a strong mechanical strength that it could be used as a reinforcement in composite materials¹ whereas amorphous cellulose displays important viscoelastic properties.^{2,3} In turn, the ability to form various ultrastructural organizations depends on both the conformational characteristics of the individual chains and their interactions in the solid state. It is therefore of importance to characterize the organization of the chains in both their crystalline and amorphous states.

Crystalline cellulose has been studied for many years.⁴ The main structural contribution comes from CP/MAS ${}^{13}C$ NMR, which demonstrates that the crystal phases of native cellulose samples are always a composite of two allomorphs, named $I\alpha$ and $I\beta$.⁵ Electron diffraction allows us to define their space group and cell dimensions.⁶ This structural polymorphism has complicated the quantitative analysis of the X-ray diffracted intensities; it is therefore very difficult to obtain exact atom coordinates within the unit cells. However, the use of valonia and tunicin highly crystalline samples should lead to quantitative solutions. To complete those studies, molecular modeling has been used to find the best coordinate set within the unit cells that is consistent with both diffraction data and total potential energy.^{7,8} Altogether these studies allow us to get an overall realistic

picture of the crystal structures. In short, individual chains are formed by a helix having two residues per turn and a pitch of 10.34 Å. They are aligned parallel and are shifted about 1/4 of the cell in the direction of the fiber axis. The two chains of the monoclinic phase are not equivalent, the central chain is slightly rotated with respect to the corner chain. Chains are organized in sheets whose cohesion depends on hydrogen bonds that are revealed by vibration spectroscopy.^{9,10} Sheet stacking is stabilized by van der Waals forces.

In contrast to the huge efforts to characterize crystal structures of cellulose, the amorphous phase suffers from the lack of structural studies. The absence of long range order is evidenced by wide-angle X-ray scattering (WAXS)¹¹ and SAXS.¹² Comparing IR spectra of amorphous cellulose derivatives, differing in the substitution pattern, emphasizes the important role of the O2 and O3 hydroxyls in the hydrogen bonding network (see Figure 4 for the atom numbering). Solid-state NMR on different samples varying in crystallinity shows that the amorphous or paracrystalline (the crystal surface chains) zones exhibit a spectral signature.^{13,14} Molecular mobility within these regions is homogeneous and larger than the mobility of the chains that are within the crystal, as seen with inelastic neutron scattering studies.¹⁵ Structural information on amorphous cellulose is therefore limited and, for example, important characteristics such as the glass transition temperature have never been precisely measured.

Molecular modeling is a well adapted technique to investigate the organization of the cellulose chains within the material. Here again, most of the efforts have been devoted to model the crystal phases. Modeling protocols go from simple minimizations of finite-sized systems (without periodic boundary conditions) to

* Corresponding author. E-mail: karim.mazeau@cermav.cnrs.fr.

molecular dynamics experiments performed on infinite solids with periodic boundary conditions. Former studies, called “minicrystals”, allowed prediction of the relative stability of the different cellulosic allomorphs.^{16–18} However, significant uncontrolled edge effects are expected in such computations. Later studies use molecular dynamics; they can be divided in two groups: those performed in the canonical (NVT) ensemble and those performed in the isobar-isothermal (NPT) one. NVT molecular dynamics computations have been performed on different crystalline forms to reveal structural and energetic data^{19,20} or their interconversions.²¹ However, NVT computations constrained the volume of the simulated system; it is therefore not possible to access cohesive and thermodynamic properties of cellulose; in particular, one cannot predict the equilibrium density of the system, which is nevertheless a choice criterion for evaluating the suitability of the modeling results. Furthermore, a solid system modeled like that might be mechanically unstable. Finally, NPT molecular dynamics is well suited to model solid structures. Modeling of native cellulose phases were performed^{22–26} with the aim of predicting their elastic moduli. Densities are of the same order of magnitude as those experimentally measured and structural details given are limited to the most abundant hydrogen bonds: intrachain (O5–O3) and (O6–O2) and interchain intrasheet (O6–O3). Surprisingly, the structure and dynamics of crystalline native celluloses was not investigated in detail by those early computational NPT experiments.

To our knowledge molecular modeling of the amorphous cellulose in the bulk state has never been reported. Based on Flory’s hypothesis,^{27,28} the Theodorou–Suter method²⁹ models the glassy state by an ensemble of cubic cells with periodic boundary conditions, those cells being filled by a nonperturbed chain. The cube is then considered as a part of an infinite medium, consisting of displaced images of the same chain. In this paper, solid models of cellulose have been generated and simulated under the NPT ensemble. We have characterized the bulk native I α and I β crystal phases together with an anhydrous amorphous phase. Comparison between the available experimental data on model crystal structures and their predicted characteristic allows us to estimate the reliability of the force field to model those systems. For the first time an amorphous cellulosic solid is modeled; ultrastructural organization, cohesive properties, and fundamental differences between amorphous and native crystalline phases are reported.

2. Material and Methods

Energy calculations were carried out by using the second-generation force-field PCFF^{30–34} specially suited for polymers and other materials. The PCFF force field is an augmented version of the *ab initio* consistent force field (CFF91) for which new functional groups were added. The CFF91 force field has been parametrized and validated using condensed phase properties in addition to various *ab initio* and empirical data for molecules in isolation. The bound terms of the potential energy function include a quadratic polynomial for both bond stretching and angle bending, a three-term Fourier expansion for torsions, and a Wilson out of plane coordinate term. Six crossterms up to the third order are present to account for coupling between the intramolecular coordinates. The final two nonbonded terms use a Coulombic form for the electrostatic energy and an inverse 6–9th power Lennard-Jones function is used for the van der Waals term. For the Coulombic term, the dielectric constant value was set to 1. All atoms are treated explicitly.

2.1. Structure Generation. Typically, the polymer is represented as an ensemble of cubic microscopic structures for

which periodic continuation conditions are employed. Those microstructures are a part of an infinite medium that adequately models solids. Three systems are considered in our study: the two native I α and I β crystallographic phases and an amorphous solid; they are presented in Figure 1.

2.1.1. Crystalline Microstructures. The chain conformations and cell dimensions were based on a previous study.¹⁸ A schematic representation of cellobiose, the building block of cellulose is given in Figure 4.

The computational box consists of $3 \times 3 \times 2$ unit cells. Coordinates of cellulose chains along with periodic images are generated and positioned in a crystalline supercell subjected to periodic boundary conditions in all three directions. The edge dimensions of the supercell is exactly the sum of all the elementary cells that were used. The models of the I α and I β consist of 16 and 18 chains, respectively. The degree of polymerization of each chain is 4; therefore the computational systems consists of 32 cellobiose units for I α and 36 for I β . However, to model infinite chain length, the glucose residues are covalently bonded across the periodic box in the direction of the chain axis. Symmetry and crystallographic translations are not fixed within the computational box.

2.1.2. Amorphous Microstructures. In the conformational analysis of polymers, Flory^{27,28} stated that a polymer in a condensed amorphous state exists in a nonperturbed conformation. This hypothesis imposes that the torsion angles of each glycosidic bond experience values characteristic of those computed for the isolated dimeric fragment. Furthermore, it was often observed that, for the modeling of the amorphous solids, the geometry of the final equilibrated system is close to that of the initial system. Only minor conformational variations are observed during the whole equilibration process. It is therefore important to reproduce the conformational preferences of cellulose at the generation step.

There are many reports on the conformational analysis of cellobiose in the literature; for example, see ref 35. The potential energy surfaces of cellobiose show that the *gauche* orientations of the Φ torsion angle are preferred. Furthermore, the *gauche*— (between 240° and 300°) orientation leads to more favorable conformers than *gauche*+. Orientation *trans* of this angle only corresponds to a conformational transition barrier. On the other hand, all the staggered orientations of the Ψ torsion angle are accessible. For the generation of the amorphous microstructures, the torsion angle ϕ is restrained to a unique value of 270° whereas all three staggered states at 60°, 180°, and 300° are considered for the torsion angle ψ . Finally, values for torsion angle ω are randomly assigned. For those generated structures, the torsion angles are allowed to be dispersed by 20° around their canonical values.

The first repeat unit is filled into the box by choosing place and orientation at random. Then, a random conformation of a polymer is built one residue at a time within the cell. A conformation is accepted if the generated residue is free of strong steric clashes with all the previously generated ones. As segments were added to the growing chain, the nonbond distances of the conformation generated were checked. To facilitate the generation of the polymer within the box, a scale factor of 0.3 was applied to all the van der Waals interactions in this first stage of the generation. The minimum nonbond distance allowed is equal to the sum of the two atom’s van der Waals radii multiplied by this specified scale factor.

The glucopyranose unit was built *ab initio* from standard values of the internal geometrical parameters: bond lengths, bond angles, and torsion angles. Three chain lengths were tested, with

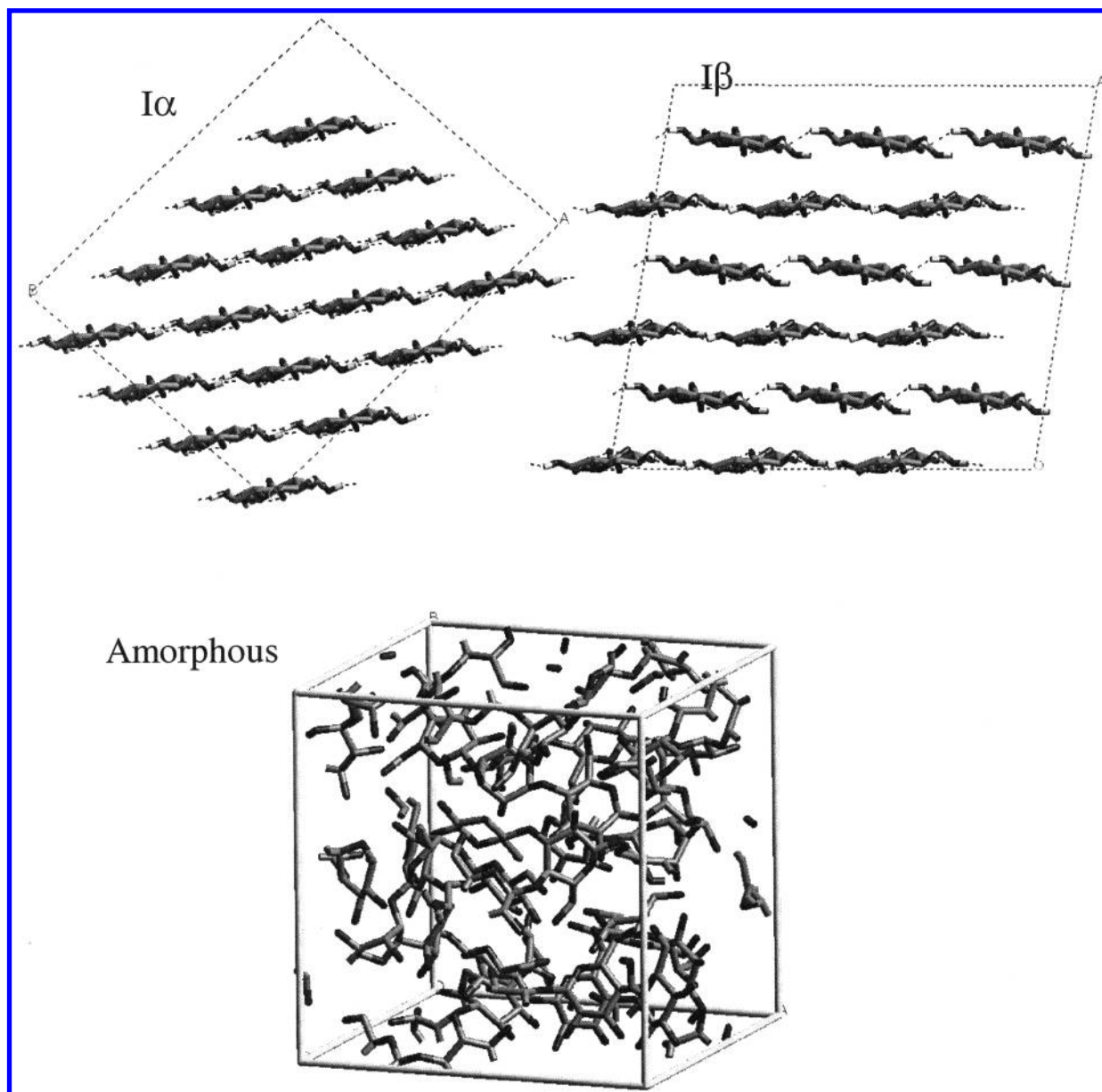


Figure 1. Modeled microstructures.

dP 10, 20, and 40, respectively. Computational boxes of dP 10 include four chains, those of dP 20 only two and finally only one chain is considered for the systems of dP 40. Also two different initial densities of 1.5 and 1.8 g/cm³ were considered. The results appear to be independent of both initial chain length and initial density. We have therefore used a unique chain of dP 40 because high dP are conceptually better models of cellulosic chains and the initial density was set to 1.5 g/cm³.

An amorphous ensemble containing four independent conformations is constructed.

2.2. Structure Equilibration. The goal of this step is double. First the structure should correspond to an energy minimum of the potential energy and second it should be free of internal tension or compression. Each generated structure is then relaxed. This process of minimization was performed by, first, the steepest descents and, second, the conjugated gradient method. However, a straightforward molecular mechanics scheme is likely to trap the simulated system in a metastable local high-energy minimum. Molecular dynamics simulation was used to prevent the system from such entrapments by providing thermal energies to cross energy barriers between local minima. A

relaxation cycle was used, consisting of a 5 ps NVT dynamics run in which the temperature is maintained at 800 K, followed by an energy minimization run, 20 ps NVT at 600 K, and minimization. Then another 20 ps dynamics at 400 K was performed in the NPT ensemble in which the simulation box was allowed to vary in size and shape. This was again followed by an energy minimization.

Our purpose in using short-run molecular dynamics and minimization in this investigation is to relax the bulk structure efficiently. The convergence criteria used for energy minimizations was a root-mean-square (rms) force less than 0.1 (kcal/mol)/Å for the polymer and 0.1 (kcal/mol)/Å³ for the stresses on the periodic boxes. Both convergence criteria were simultaneously satisfied for the system to be relaxed completely.

2.3. Molecular Dynamics. Each simulated microstructure was then subjected to energy minimization before the actual molecular dynamics simulation was started. The simulations were carried out for 400 ps each after another 100 ps equilibration time.

The standard Verlet³⁶ algorithm was used to integrate Newton's law of motion with a time step of 0.001 ps. For the

TABLE 1: Average Internal Stress Components (MPa) of the Generated Microstructures

stress	I α	I β	am1	am2	am3	am4
XX	-0.0114	-0.0121	-0.0100	-0.0102	-0.0093	-0.0093
YY	-0.0122	-0.0069	-0.0095	-0.0102	-0.0108	-0.0108
ZZ	-0.0108	-0.0091	-0.0103	-0.0107	-0.0109	-0.0109
YZ	-0.0010	0.0006	0.0003	0.0009	0.0000	0.0000
XZ	-0.0011	-0.0002	0.0003	-0.0001	-0.0002	-0.0002
XY	-0.0018	0.0000	-0.0003	0.0005	-0.0002	-0.0002

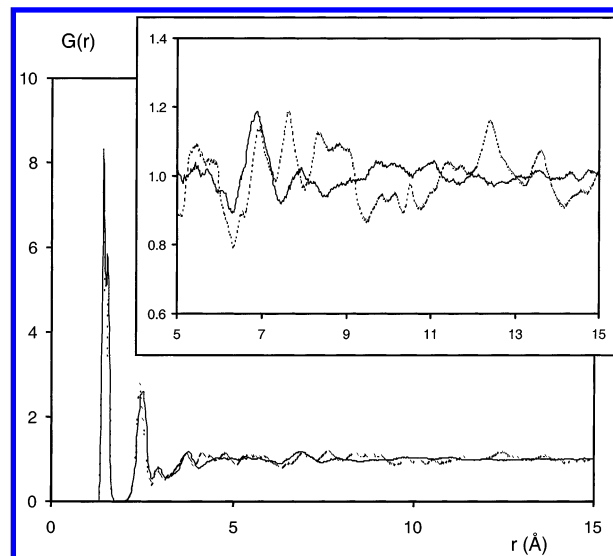
canonical NPT dynamics,³⁷ the relaxation time constant and the masslike parameter, which determines the rate of change of volume/shape matrix, were set to 0.1 ps and 1.00, respectively. Each molecular dynamics run was started by assigning initial velocity for the atoms according to a Boltzmann distribution at $2T$, T being the target temperature. The velocities of the atoms were quickly scaled down so that the final temperature of the atoms was T . The total external pressure was maintained at 1 atm., and Nose's algorithm³⁸ was used to keep the cell temperature constant at 300 K in the molecular dynamics simulation. The pressure and temperature used in our simulation are convenient computational parameters to relax the model polymer and are not intended to reproduce the actual thermodynamic state (P , V , T) of the real polymers.

All calculations were performed at the Centre d'Expérimentation et de Calcul Intensif, CECIC, Grenoble.

3. Results and Discussion

3.1. Stress Tensors. The simulated structures must satisfy the criterion that the values of the internal stresses must be (close to) zero, which means that the structure reaches a local minimum of the potential energy surface and ensures thus an equilibrium state. The components of the internal stress tensor are defined as the first derivatives of the potential energy per unit volume with respect to strains. Table 1 shows the values of different stress components for the I α and I β crystal structures and for the four amorphous samples. The values of the stress components clearly indicate that the polymer chains are mechanically relaxed.

3.2. Radial Distribution Functions. The atomic pair distribution function, $g(r)$, can help to investigate dense structures, it gives a measure of the order in the system by calculating the spatial orientation of the atoms. To evaluate this function, the simulated boxes have been doubled in each direction and equilibrated following the same procedure. $g(r)$ is then calculated for an integration step 0.1 Å and for 0–15 Å. Because the molecules contain different atoms, a set of all the correlation pairs between heavy atoms is required to completely characterize the system. The pair distribution function for the simulated crystal I β phase and for an amorphous sample are shown in Figure 2. A first inspection of the global behavior of both $g(r)$ shows no visible difference between the crystalline and the amorphous structure. Both structures share all the important peaks that appear at short distances. The peaks at distances less than 2 Å arise due to chain connectivity. The peaks at 1.44 and 1.55 Å are assigned to covalently bound C–O and C–C atoms, respectively. Peaks that occur at distances greater than 2 Å are due to nonbonded atoms separated by two, three, and four bonds on the chain. This structural order due to intramolecular connections disappears at longer distances. Significant differences between the $g(r)$ profiles of the crystalline and the amorphous structures appear at larger distances, above 5 Å. We have therefore enlarged the 5–15 Å region, which is displayed in the inset in Figure 2. In the crystalline microstructure peaks fluctuate with a large amplitude; this fluctuation is still

**Figure 2.** Radial distribution functions of the crystal I β (dashed) and amorphous (bold) structures. The inset is an enlargement of the 5–15 Å section.**TABLE 2: Equilibrium Densities (g cm⁻³), Average Values and Standard Deviations, of the Generated Microstructures**

density	I α	I β	am1	am2	am3	am4	Am
average	1.5806	1.5577	1.3414	1.3927	1.3853	1.3853	1.3762
sd	0.0022	0.0006	0.0005	0.0009	0.0025	0.0025	0.0016

perceptible at 15 Å, whereas the amorphous $g(r)$ profile is damped as early as 9 Å.

Absence of peaks at large distance for the amorphous structure indicates that there is no long-range order in the sample. This spatial distribution function represents thus a randomized structure. In contrast, the presence of peaks over a large distance for the crystalline $g(r)$ profile implies the existence of a longer range order in the structure.

3.3. Density. Because the cell parameters are allowed to vary during molecular dynamics experiments, the density can therefore vary. Density is a relevant parameter to evaluate the realism of the simulated microstructures; values are reported in Table 2. The predicted equilibrium density, of 1.58 and 1.56 g cm⁻³ is larger for the crystalline structures than for the amorphous ones. The calculated density for each of the four amorphous microstructures is remarkably constant, in the range 1.34 and 1.39 g cm⁻³. The average value is 1.3762 g cm⁻³.

The polymer handbook³⁹ indicates that the density of cellulose in cotton ranges between 1.545 and 1.585 g cm⁻³. Both crystalline phases together with amorphous phases coexist in this semicrystalline material. The reported density is an average macroscopic quantity that is not directly comparable with the simulated microstructures. To overcome this problem, densities corresponding to the crystallographic phases can be estimated from the reported cell dimensions.⁶ From those values, the experimental densities are 1.582 and 1.599 g cm⁻³ for the I α and the I β phases, respectively. The predicted density of the I α allomorph is therefore very well predicted and the one of the I β allomorph is slightly lower by less than 3% of the expected value. As a general trend for the polymer, the density of the amorphous phase is expected to be 10–20% lower than that of the crystalline phase. The density of the amorphous systems should then be in the range of 1.28 and 1.44 g cm⁻³. Our models agree well with this general consideration.

3.4. Crystalline Cell Parameters. Refining both the molecular and cell geometries of the initial crystalline models did

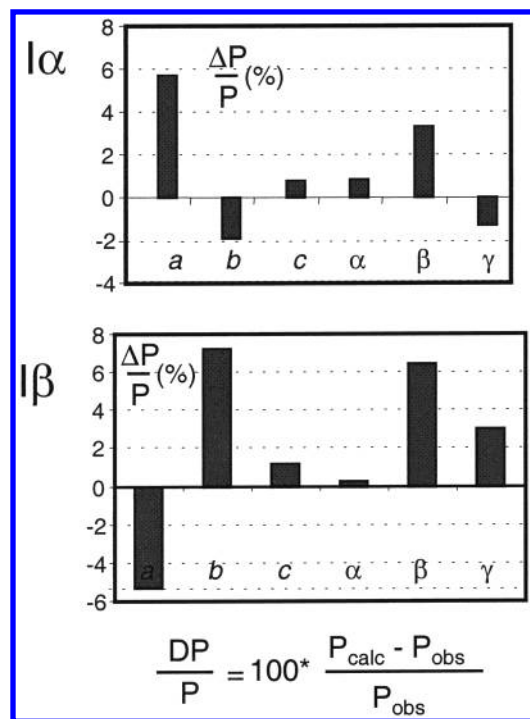


Figure 3. Deviation of the crystalline unit cell parameters with respect to the experimental values.

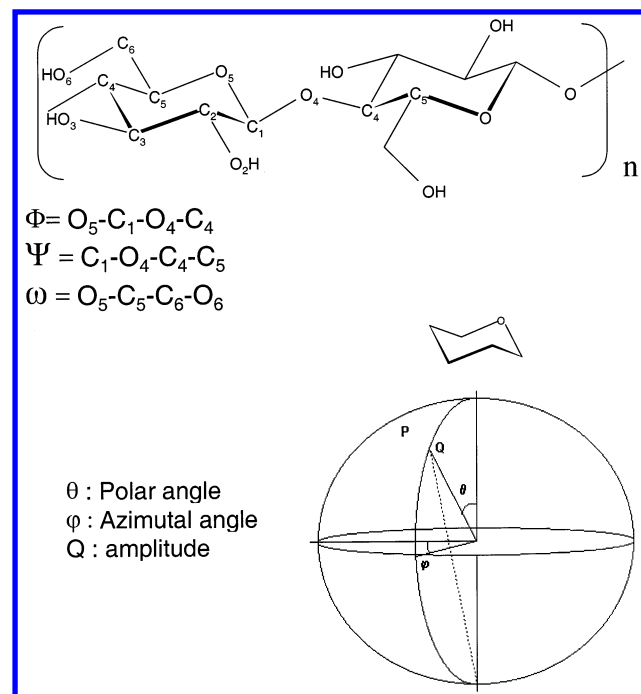


Figure 4. Conformational parameters of cellulose.

not induce major changes in the packing arrangements. Deviation between the expected⁶ and predicted values of the cell parameters for the crystalline structures are displayed in Figure 3. Deviations in cell lengths and angles are reasonably small even though full cell optimizations were performed. For the $I\beta$ form, a narrowing of the a axis and an expanding of the b axis is observed; the opposite behavior could be observed for the $I\alpha$ crystal. In both allomorphs, the fiber axis (dimension c) is remarkably close to the optimal value and corresponds to the maximal extension of the chain.

The largest deviation between experimental and calculated cell geometry amounts to 7%. This deviation fits well within the expected error margin of force field methods together with

TABLE 3: Energies (kcal/mol per Cellobiose Unit) and Energy Components of the Simulated Microstructures

	$I\alpha$		$I\beta$		Amorphous	
	average	sd	average	sd	average	sd
potential	-190.29	25.18	-231.70	29.24	-202.16	27.54
VW	12.87	22.14	8.87	19.20	15.12	23.37
electro	-220.43	40.74	-267.41	38.70	-252.10	34.38

Average values and standard deviations (sd).

TABLE 4: Volumes (\AA^3), Cohesive Energy Densities ((kcal/mol)/ cm^3) and Solubility Parameters (J/cm^3)^{1/2} for the Simulated Microstructures

	$I\alpha$	$I\beta$	amorphous
vol	11389	14752	7817
CED	0.735	0.752	0.672
δ	71.44	72.27	68.33

the experimental uncertainty in the measurement of the cell dimensions. The degree of conservation of the unit cell parameters is an indication of the compatibility of the simulated model with experimental diffraction data and therefore of the suitability of the force field.

3.5. Energetics. Table 3 gives the total potential energy and their nonbonded components for each modeled system. For the crystallographic microstructures, the $I\beta$ allomorph is computed more stable than the $I\alpha$ form by 40 kcal mol⁻¹ disaccharide⁻¹. The average potential energy of the amorphous structures is between the two crystallographic forms; it is more stable than the $I\alpha$ form and less stable than the $I\beta$ one. Splitting the total potential energy into its nonbonded (van der Waals and electrostatic) and bonded components shows that the electrostatic term is the most important one. van der Waals interaction is positive and very weak as compared to the large and negative electrostatic term.

The cohesive energy is a widely used quantity for characterization of polymeric systems. It is defined as the ensemble average of the intermolecular part of the internal energy per mole of substance. The cohesive energy density corresponds to the cohesive energy per unit of volume, and Hildebrand's solubility parameter, δ , is the square root of the cohesive energy density. Table 4 gives the cohesive energies densities and solubility parameters together with the volumes of each simulated system.

The cohesive energy density is dependent on the supra-molecular organization of the cellulosic chains; the computed systems displays a 17 kcal mol⁻¹ cm⁻³ difference between the crystalline phases, and a difference of 63 kcal mol⁻¹ cm⁻³ is also observed between the amorphous and crystalline $I\beta$ phase. The $I\beta$ allomorph is the most stabilized by intermolecular interactions, followed by the $I\alpha$ form, and the amorphous structures are the less stabilized.

All those results are consistent with experimental hydro-thermal conversion of cellulose: it is possible to convert crystalline $I\alpha$ cellulose into crystalline $I\beta$ form.⁴⁰ The $I\alpha$ allomorph is necessarily less stable than the $I\beta$ one.

Methods used for the determination of Hildebrand's solubility parameter are numerous: calculation using group molar attraction constants,⁴¹ solubility measurement in solvents of known properties,⁴² indirect measurements from known relationships with either surface free energies,⁴³ or mechanical tensile modulus^{41,44-46} or interaction measurements using inverse gas chromatography.⁴⁷ Indirect measurements give solubility parameter values in the range 48–56 (J cm^{-3})^{1/2}, whereas the group contribution method gives 62 (J cm^{-3})^{1/2} and the interaction measurement 80 (J cm^{-3})^{1/2}, respectively. This

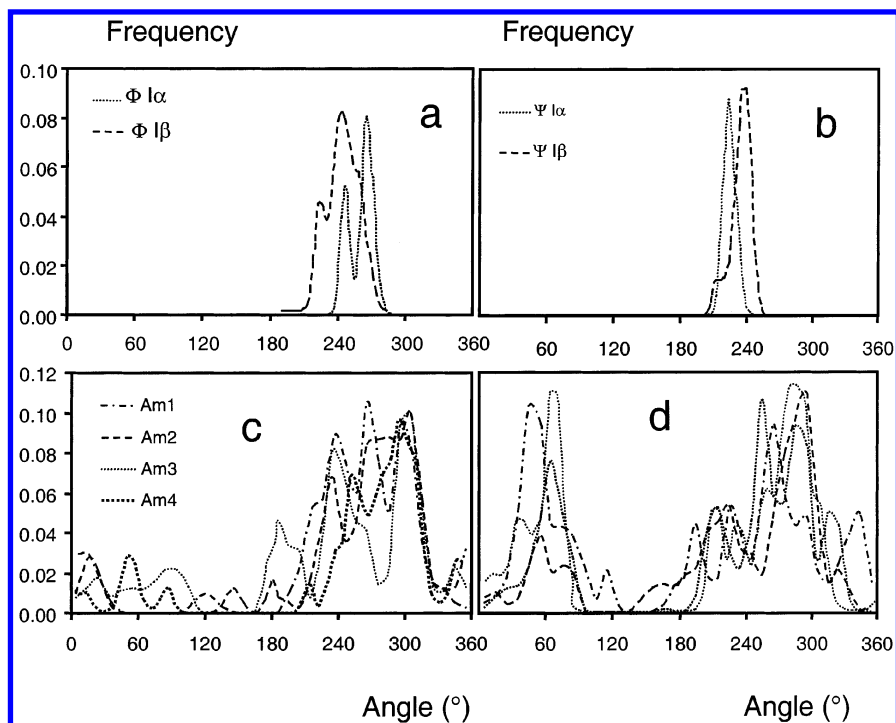


Figure 5. Glycosidic angles distribution for the crystalline structures (a, Φ ; b, Ψ) and for the amorphous structures (c, Φ ; d, Ψ)

emphasizes the difficulty to evaluate the cohesive energy density for cellulose. Indeed, the results will depend on the initial ultrastructure of the cellulosic sample, including defects and accessibility. Our results are reasonably situated between the group contribution and interaction measurement values. They especially point out the very small differences that exist between the three structures. This is in agreement with the observed coexistence of $I\alpha$ and $I\beta$ phases in the same crystal structure.

As an additional indication of the suitability of the force field to model such molecules, the same type of measurements have been performed on simpler polymers, PAA and PVA, that have in common with cellulose the large number of pendant hydroxyl groups.⁴⁸ The reported experimental value for the solubility parameter of the well-known PVA is $53 \text{ (J cm}^{-3})^{1/2}$.⁴⁹ The corresponding predicted values using the same force field 51 and $57 \text{ (J cm}^{-3})^{1/2}$ for amorphous i-PVA and s-PVA, respectively. The same calculation leads to values of 52 and $53 \text{ (J cm}^{-3})^{1/2}$ for the relaxed i-PAA and s-PAA, for which no experimental data are available.

3.6. Geometrics. Figure 4 gives all the structural parameters that we have considered: torsion angles across the glycosidic bonds, orientation of the hydroxymethyl group, and pyran ring puckering. Rather than presenting traditional trajectories of how a structural parameter changes over time, we collected and binned the angle parameters into 10° units. The results are then presented as a graph that contains the distribution of the parameter over the entire simulation time period. This illustrates the number of visits of the angle made to a particular range during the simulation.

3.6.1. Torsion Angles about the Glycosidic Bonds. The distributions of the Φ ($O5-C1-O1-C4'$) and Ψ ($C1-O1-C4'-C5'$) glycosidic torsion angles are displayed in Figure 5. Parts a and b of Figure 5 are those of the two crystalline phases.

For the two crystalline microstructures (Figure 5a,b) the Φ and Ψ torsion angles are all located in the g^- angular domain, which corresponds to conformations of maximal extension. Two populations of the Φ angle, centered on $(230^\circ, 247^\circ)$ and $(247^\circ, 265^\circ)$ for the $I\beta$ and $I\alpha$ forms, respectively, can be seen in Figure

5a. Two potential wells can therefore be identified within this angular domain. These two potential wells are differently populated because the width and the height of the peaks differ. The Ψ torsion angle is centered at 224° and 240° for the $I\alpha$ and $I\beta$ allomorphs, respectively.

Conformational disorder of the cellulose chains is suggested by these results. Helices slightly diverge from the perfect 2_1 conformation. On one hand, the glycosidic torsion angles values within the modeled crystal microstructures are conventional. All the crystallographic observations of cellulose indicate that these angles explore the same angular domain.⁴ Dispersion of the values was observed in the crystal structures of model cello-oligosaccharides solved by direct methods. In particular, two different crystal structures of cellotetraose^{50,51} report limiting values in the range $(261^\circ, 271^\circ)$ and $(207^\circ, 218^\circ)$ for the Φ and Ψ torsion angles, respectively. On the other hand, it was observed that the potential energy surface of cellobiose possess two wells, perfect 2_1 helices are localized exactly between these two wells, on the conformational transition barrier.¹⁸ It is interesting to note that the helices modeled here explore alternatively one then the other of the two wells. This behavior ensures a larger stability of the system and is compatible with the extension of the chain of around 10.4 \AA per cellobiose.

Unlike the crystalline models, the glycosidic torsion angles of the amorphous models span the whole angular range (Figures 5c and 5d). Fine details of the profiles are structure dependent but a general behavior can be observed. Maximal concentration of the Φ torsion angle lies between 220° and 320° , other values of this angle are of minor importance. Values that are the most explored by the Ψ torsion angle belong to two distinct conformational domains, between 40 and 100° and between 200° and 320° .

To our knowledge, no experimental measurements of the torsion angles of the amorphous cellulose have been reported. General characteristics of the potential energy surface of cellobiose³⁵ are however correctly reproduced. Accessible values of the torsion angles of the glycosidic bond depend on both steric (torsion angle Ψ) and stereoelectronic (angle Φ) interac-

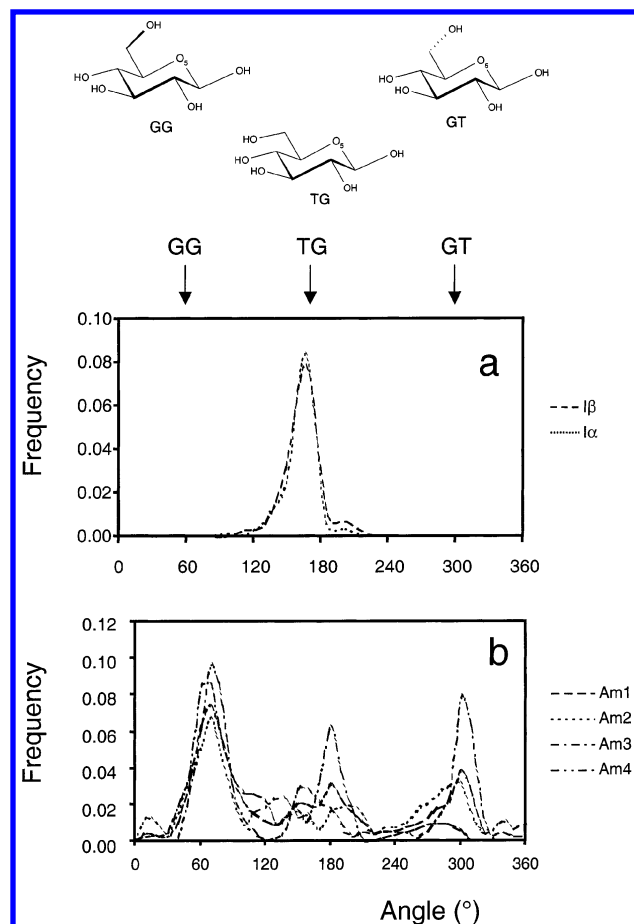


Figure 6. Torsion angle ω distribution for the crystalline (a) and amorphous (b) structures.

tions.⁵² The main accessible area of the potential energy surface of cellobiose is located at the g^- angular range of both Φ and Ψ torsion angle. Two other potential energy wells could be distinguished on the map, at (g^-, g^+) and (g^+, g^-) of the Φ and Ψ angles. Our calculated data are in good agreement with these observations.

3.6.2. Hydroxymethyl Group Conformation. Every glucopyranose unit possesses a hydroxymethyl group whose orientation is described by the ω torsion angle. Typically, in the carbohydrate nomenclature the three staggered orientations of this group are commonly named gg, tg, and gt corresponding to ω values of 60° , 300° , and 180° , respectively. Figure 6 gives the populations visited by the torsion angle ω for the crystalline (Figure 6a) and amorphous (Figure 6b) model microstructures.

Values are distributed around a unique tg orientation for the crystal forms. Notwithstanding there is no direct experimental measure of the orientation of the hydroxymethyl in the crystal structure of native cellulose, the tg orientation is generally accepted.⁵³ Molecular models of native cellulose crystals agree better with experimental diffraction data when the hydroxymethyls are in the tg orientation. Furthermore, empirical interpretation of the solid-state NMR C6 chemical shifts also favors the tg orientation,⁵⁴ which is typical of native cellulose.

The whole angular range is explored for the amorphous models, largest populations are located in the staggered orientations whereas the eclipsed ones have negligible abundances. Unlike the native crystalline structures, the most important angular domains corresponds to the gg and gt ones; note that only one amorphous microstructure shows a nonnegligible population of the tg state. Here again there is no experimental

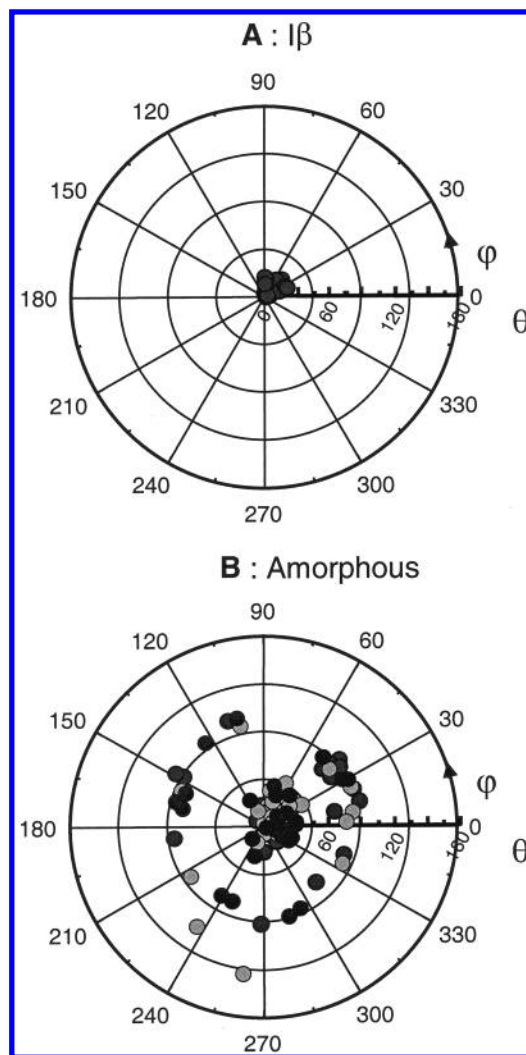


Figure 7. Puckering angles parameters for the crystalline $I\beta$ (a) structure and the amorphous (b) structures.

data on amorphous celluloses; however conformational behavior of the hydroxymethyl is well documented.⁵³ Statistical analysis of the glucose containing crystals together with NMR data has stated that the gg:gt:tg orientations are populated at 60, 40, and 0%, respectively. This corresponds roughly to our observations. The gg and gt orientations in which the O6 and O4 oxygen atoms are not in the 1,3 diaxial position are preferred to the tg one. In the tg orientation those two atoms are in a repulsive steric and electronic interaction. As far as we know, this specific conformation only occurs in the native state. Our results perfectly reproduce those conformational preferences.

3.6.3. Puckering of the Glucopyranose Rings. The most stable conformation of the six-membered ring glucopyranose systems is the 4C_1 chair form. This chair conformer is more stable than the others. However, the pyranoid ring can also adopt energetically less favorable conformations. Six different skew conformers separated by six different boat conformers can be identified on the pseudorotational itinerary of a pyranoid ring. Three puckering parameters⁵⁵ define unambiguously the position of the individual forms of the pyranoid ring on the conformational sphere, Q is the maximum puckering amplitude, the parameters θ and φ are angles in the range $0^\circ < \theta < 180^\circ$ and $0^\circ < \varphi < 360^\circ$, and can be thought of as polar and azimuthal angles for a sphere of radius Q . Analysis of the calculated data shows that the Q parameter is constant at about 0.62 \AA . The results can then be presented graphically by a circle that corresponds to

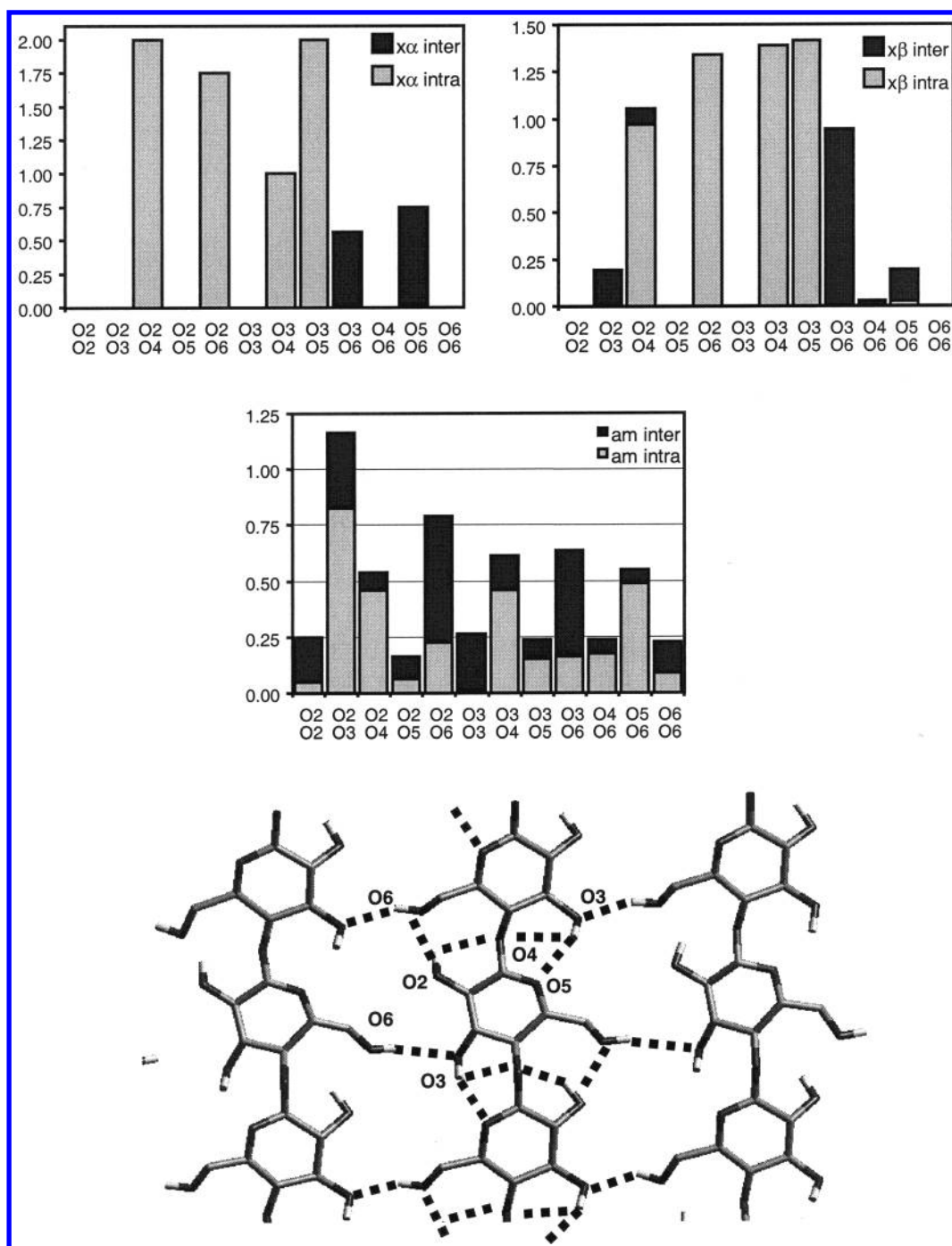


Figure 8. Hydrogen bonds statistics for the crystalline structures and the amorphous (a) structures and drawing of the typical inplane hydrogen bonds of the crystalline structures.

the projection of the sphere on a surface along the north to south axis. Variations of the θ parameter are seen on those figures by the distance with respect to the center of the circle, whereas the angular position represents the φ parameter. The classical 4C_1 ring conformation is located exactly at the center of the circle.

Pyranose puckering of the $I\beta$ crystalline allomorph is shown in Figure 7a (identical results were obtained for the $I\alpha$ phase) and those of the amorphous structures are presented in Figure 7b.

All the pyranoid rings adopt conformations close to the classical 4C_1 chair in the crystal structures. In contrast, two distinct families of conformations can clearly be distinguished on Figure 7b. For the amorphous structures, on average 73% of the rings are exploring the most favored conformation 4C_1 .

The 27% remaining rings explore less stable conformations for which the polar angle is nearly constant at 90° and the azimuthal angle is almost free. To check the ability of the force field to correctly reproduce the glucopyranose classical chair form, an isolated chain of cellulose was modeled. The results shows that all 40 rings are grouped in a unique conformation close to the canonical 4C_1 , at puckering parameters ($Q = 0.6 \text{ \AA}$, $\theta = 5^\circ$, and $\varphi = 339^\circ$).

Such distortions of the pyran rings seem to be technologically and biologically very important. It is assumed that viscoelastic properties of polysaccharides are dependent on the flexibility of the pyran rings.^{56,57} High-energy distorted puckering could be stabilized in a molecular environment within the protein active site for example. Finally, unperturbed average chain dimensions have never been correctly predicted in the case of

cellulose. It is assumed that the systematic gap between numerical simulations and experimental data might originate from ring puckering.^{58,59} Even if such distortions are infrequent events, they induce large changes in the direction of the chain propagation and thus in the global geometrical characteristics.⁶⁰

3.7. Hydrogen Bonds. As aforementioned, intermolecular stabilization is dominated by electrostatic interactions; hydrogen bonds that could be formed between the numerous oxygen atoms therefore play an important role. Hydrogen bonds could be detected from geometrical criteria; two oxygens will be considered hydrogen bonded if their distance is smaller than 2.5 Å and the angle donor–hydrogen...acceptor larger than 120°. Figure 8 gives the number of hydrogen bonds for all the oxygen atom pairs together with a molecular drawing that shows the typical in plane hydrogen bonds of the crystalline structures. All types of oxygen atoms are hydrogen bonded in either the amorphous or crystalline microstructures. However, the total number of hydrogen bonds per residue is larger for the crystalline microstructures than for the amorphous ones. The total number of hydrogen bonds per repeat unit of cellulose reaches 8 and 6.5 for the crystalline I α and I β forms whereas, on average, every glucosidic unit of the amorphous structures forms only 5.3 hydrogen bonds.

More interestingly, the hydrogen bond characteristics differ in a qualitative way between the different microstructures. To go further into detail, one has to distinguish between intramolecular hydrogen bonds, which stabilize the helical conformation of the cellulose chains, and the intermolecular hydrogen bonds, which participate in the sheet cohesion in the crystalline structures. The I α and I β phases particularly differ in the characteristics and number of their intermolecular hydrogen bonds, which are larger in the I β phase. Indeed, this latter allomorph is stabilized alternatively by recurrent (O2–O6) and (O3–O6) hydrogen bonds, whereas the I α phase displays a looser network of intermolecular hydrogen bonds between (O3–O6) and (O5–O6). This particular repartition of the intermolecular hydrogen bonds has consequences on the occurrence of the intramolecular hydrogen bonds, which are less relevant for the stabilization of the crystalline structure. For example, the low occurrence of the intramolecular pair (O5–O6) is not compatible with the intermolecular pair (O3–O6); both are in competition. In the I α phase, the number of intramolecular (O2–O4) and (O3–O5) pairs is maximum, whereas (O3–O4) and (O3–O5) intramolecular hydrogen bonds are the most represented in the I β phase. Note that for both crystalline phases, the number of intermolecular hydrogen bonds is never maximum, indicating a certain degree of disorder.

The case of the amorphous phase is slightly different, as the notion of stabilization of the helical conformation or the sheet cohesion is irrelevant. For this amorphous structure, all possible oxygen atom pairs are hydrogen bonded, in contrast with the crystalline ones for which systematic absences could be detected. This is the result of conformational disorder already pointed out in a preceding section. Moreover, the presence of a new type of intramolecular hydrogen bond such as (O2–O3) should stabilize conformations that are not explored in the crystalline phases.

IR spectroscopy is the best physical technique to access the hydrogen bonding scheme in solids. Two independent studies have been reported. The first study⁶¹ stated that the O2 and O3 oxygen atoms are very important in the amorphous phase whereas O6 atoms mostly form hydrogen bonds in the crystalline phase of the material. Our results emphasize the major role of the O2 and O3 atoms in the amorphous phase; they reveal,

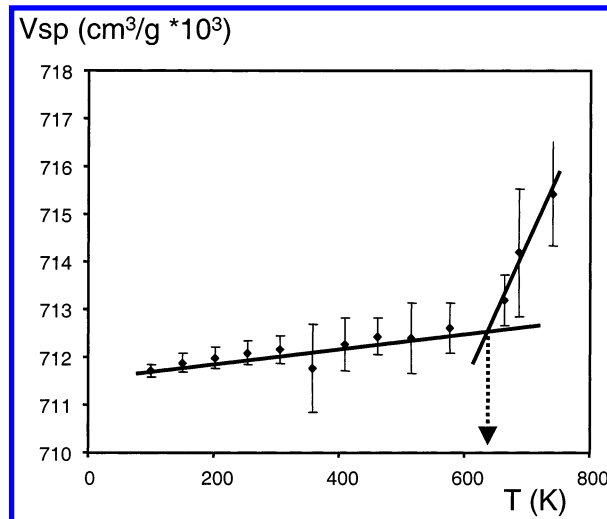


Figure 9. Specific volume variations as a function of temperature.

however, that O6 atoms can be involved in hydrogen bonds in this amorphous phase. Furthermore, our results qualitatively agree with the hydrogen bond network deduced from the deep analysis of the IR spectra of the crystallographic I β allomorph.⁹

3.8. Glass Transition Temperature. The glass transition temperature is a fundamental property of amorphous materials. In the case of cellulose, this parameter is not well established. To complete the experimental approaches, molecular modeling can help in estimating this parameter. From a thermodynamic point of view, the glass transition temperature appears as a change in the slope of the specific volume versus temperature. With this aim, NPT molecular dynamics experiments at different temperatures have been performed on a randomly selected amorphous microstructure. The variation of the specific volume with temperature appears in Figure 9. As expected, linear variations are observed on both sides of a critical temperature. This temperature should correspond to the glass transition temperature, it is estimated at about 650 K. To compare with experimental results, one has to remember that the glass transition is kinetic by nature, so that this value will strongly depend on the time scale at which the measurements are performed. In our case, the 400 ps dynamics roughly correspond to frequencies on the order 2 MHz. This means that T_g should be around 40 K higher compared to what should be obtained with classical differential scanning calorimetry experiments.

However, no direct experimental measurements of the glass transition temperature of dry amorphous cellulose are available in the literature. The main reason is that the temperature range at which the main relaxation occurs is close to the degradation temperature of the material. Indirect estimations of this temperature has been reported by measuring T_g of chemical derivatives of cellulose. Extrapolation at zero substitution degree gives T_g of the native (unsubstituted) sample.⁶² Other authors have also measured T_g of celooligosaccharides and, again, extrapolated T_g for longer chains.⁶³ Authors have also observed the principal relaxation on hydrated samples,⁶⁴ as water acts as a plasticizer and then lowers the T_g .⁶⁵ Finally, note that some authors have reported observation of several main relaxations.^{64,66} In short, the reported experimental T_g ranges between 243 and 580 K. Any of the reported values compare favorably with the estimated T_g .

4. Conclusion

Condensed crystalline and amorphous phases of cellulose have been generated and studied by using molecular dynamics.

The low values of the stress component indicate that the modeled microstructures are mechanically stable. In agreement with a macroscopic view of the material, the radial distribution function profiles suggest that the crystallographic models exhibit correlation peaks for large distances whereas amorphous models are disorganized.

Models of both crystal allomorphs are consistent with experimental data, the density, the energy difference, all the conformational aspects, and the hydrogen bonding network reproducing reasonably well experimental observations. Inter-chain interactions within both the crystal forms and the amorphous ones seem to be correctly described as the predicted solubility parameters compare favorably with the reported values. Such an agreement suggests that the methods and strategy used are able to adequately model the amorphous phase of cellulose, which has not been so far studied so deeply. The conformational behavior of the amorphous solid differs strongly from that of the crystal phases. Torsion angles explore a very large angular range; unusual ring puckering are stabilized. An amorphous model has been used to estimate the glass transition temperature of cellulose. The predicted value is found to be larger than all the reported experimental ones.

In addition to the prediction of physical properties of the amorphous phase, like the density, the glass transition temperature, or the conformational behavior, these models could be used to investigate specific properties that are unknown for the moment, such as the permeation properties or the molecular affinity of the amorphous phase toward small molecules. The presented models will also be used in the future to model the surfaces and the interaction properties of cellulosic materials.

References and Notes

- (1) Favier, V.; Chanzy, H.; Cavaillé, J. Y. *Macromolecules* **1995**, *28*, 6365.
- (2) Montes, H.; Mazeau, K.; Cavaillé, J. Y. *Macromolecules* **1997**, *30*, 6977.
- (3) Montes, H.; Cavaillé, J. Y. *Polymer* **1999**, *40*, 2649.
- (4) Zugenmaier, P. *Prog. Polym. Sci.* **2001**, *26*, 1341.
- (5) Atalla, R. H.; VanderHart, D. L. *Science (Washington, D.C.)* **1984**, *223*, 283.
- (6) Sugiyama, J.; Vuong, R.; Chanzy, H. *Macromolecules* **1991**, *24*, 4168.
- (7) Gardner, K. H.; Blackwell, J. *Biopolymers* **1974**, *13*, 1975.
- (8) Finkenstadt, V. L.; Millane, R. P. *Macromolecules* **1998**, *31*, 7776.
- (9) Marechal, Y.; Chanzy, H. *J. Mol. Struct.* **2000**, *523*, 183.
- (10) Hinterstoisser, B.; Salmen, L. *Vibr. Spectrosc.* **2000**, *22*, 111.
- (11) Fink, H. P.; Philipp, B.; Paul, D.; Serimaa, R.; Paakkari, T. *Polymer* **1987**, *28*, 1265.
- (12) Grigoriew, H.; Chmielewski, A. G. *J. Membr. Sci.* **1998**, *142*, 87.
- (13) Wickholm, K.; Larsson, P. T.; Iversen, T. *Carbohydr. Res.* **1998**, *312*, 123.
- (14) Larsson, P. T.; Wickholm, K.; Iversen, T. *Carbohydr. Res.* **1997**, *302*, 19.
- (15) Müller, M.; Czihak, C.; Schober, H.; Nishiyama, Y.; Vogl, G. *Macromolecules* **2000**, *33*, 1834.
- (16) Aabloo, A.; French, A. D.; Mikelsaar, R.-H.; Pertsin, A. J. *Cellulose (London)* **1994**, *1*, 161.
- (17) French, A. D.; Miller, D. P.; Aabloo, A. *Int. J. Biol. Macromol.* **1993**, *15*, 30.
- (18) Victor, R. J.; Mazeau, K.; Lakin, M.; Perez, S. *Biopolymers* **2000**, *54*, 342.
- (19) Heiner, A. P.; Sugiyama, J.; Teleman, O. *Carbohydr. Res.* **1995**, *273*, 207.
- (20) Heiner, A. P.; Teleman, O. *Pure Appl. Chem.* **1996**, *68*, 2187.
- (21) Hardy, B. J.; Sarko, A. *Polymer* **1996**, *37*, 1833.
- (22) Kroon-Batenburg, L. M. K.; Bouma, B.; Kroon, J. *Macromolecules* **1996**, *29*, 5695.
- (23) Kroon-Batenburg, L. M.; Kroon, J. *Glycoconj. J.* **1997**, *14*, 677.
- (24) Marhoefer, R. J.; Reiling, S.; Brickmann, J. *Ber. Bunsen-Ges. Phys. Chem.* **1996**, *100*, 1350.
- (25) Reiling, S.; Brickmann, J. *Macromol. Theor. Simul.* **1995**, *4*, 725–743.
- (26) Neyertz, S.; Pizzi, A.; Merlin, A.; Maigret, B.; Brown, D.; Deglise, X. *J. Appl. Polym. Sci.* **2000**, *78*, 1939.
- (27) Flory, P. J. *Principles of Polymer Chemistry*; Cornell University Press: Ithaca, NY, 1953.
- (28) Flory, P. J. *Statistical mechanics of chain molecules*; Interscience: New York, 1969.
- (29) Theodorou, D. N.; Suter, U. W. *Macromolecules* **1985**, *18*, 1467.
- (30) Maple, J. R.; Dinur, U.; Hagler, A. T. *Proc. Natl. Acad. Sci. U.S.A.* **1988**, *85*, 5350.
- (31) Maple, J. R.; Hwang, M. J.; Stockfisch, T. P.; Dinur, U.; Waldman, M.; Ewig, C. S.; Hagler, A. T. *J. Comput. Chem.* **1994**, *15*, 162.
- (32) Maple, J. R.; Hwang, M.-J.; Stockfisch, T. P.; Hagler, A. T. *Isr. J. Chem.* **1994**, *34*, 195.
- (33) Sun, H.; Mumby, S. J.; Maple, J. R.; Hagler, A. T. *J. Am. Chem. Soc.* **1994**, *116*, 2978.
- (34) Sun, H. *Macromolecules* **1995**, *28*, 701.
- (35) Dowd, M. K.; French, A. D.; Reilly, P. J. *Carbohydr. Res.* **1992**, *233*, 15.
- (36) Verlet, L. *Phys. Rev.* **1967**, *159*, 98.
- (37) Parrinello, M.; Rahman, A. *J. Appl. Phys.* **1981**, *52*, 7182.
- (38) Nosé, S. *Mol. Phys.* **1984**, *52*, 511.
- (39) Brandrup, J.; Immergut, E. H.; Grulke, E. A., Eds. *Polymer Handbook*, 4th ed.; Wiley-Interscience Publication: New York, 1999.
- (40) Sugiyama, J.; Okano, T.; Yamamoto, H.; Horii, F. *Macromolecules* **1990**, *23*, 3196.
- (41) Roberts, R. J.; Rowe, R. C. *Int. J. Pharm.* **1993**, *99*, 157.
- (42) Zajic, L.; Buckton, G. *Int. J. Pharm.* **1990**, *59*, 155.
- (43) Lee, S. B.; Luner, P. *Tappi* **1972**, *55*, 116.
- (44) Bassam, F.; York, P.; Rowe, R. C.; Roberts, R. J. *Int. J. Pharm.* **1990**, *64*, 55.
- (45) Mashadi, A. B.; Newton, J. M. *J. Pharm. Pharmacol.* **1987**, *39*, 961.
- (46) Roberts, R. J.; Rowe, R. C. *Int. J. Pharm.* **1987**, *37*, 15.
- (47) Nguyen Huu, P.; Ho Nam, T.; Buchmann, M.; Kesselring, U. W. *Int. J. Pharm.* **1987**, *34*, 217.
- (48) De La Rosa, A.; Heux, L.; Cavaillé, J. Y.; Mazeau, K. *Polymer* **2002**, *43*, 5665.
- (49) Shvarts, A. G. *Kolloid Zh.* **1956**, *18*, 755.
- (50) Gessler, K.; Kraub, N.; Steiner, T.; Betzel, C.; Sandmann, C.; Saenger, W. *Science (Washington, D.C.)* **1994**, *266*, 1027.
- (51) Raymond, S.; Heyraud, A.; Qui, D. T.; Kvick, A.; Chanzy, H. *Macromolecules* **1995**, *28*, 2096.
- (52) Perez, S.; Kouwijzer, M.; Mazeau, K.; Engelsen, S. B. *J. Mol. Graphics* **1996**, *14*, 307.
- (53) Bock, K.; Duus, J. O. *J. Carbohydr. Chem.* **1994**, *13*, 513.
- (54) Horii, F.; Hirai, A.; Kitamaru, R. *Polym. Bull. (Berlin)* **1983**, *10*, 357.
- (55) Cremer, D.; Pople, J. A. *J. Am. Chem. Soc.* **1975**, *97*, 1354.
- (56) Heymann, B.; Grubmüller, H. *Chem. Phys. Lett.* **1999**, *305*, 202.
- (57) Rief, M.; Oesterheld, F.; Heymann, B.; Gaub, H. E. *Science (Washington, D.C.)* **1997**, *275*, 1295.
- (58) Brant, D. A.; Christ, M. D. *ACS Symp. Ser.* **1990**, *430*, 42.
- (59) Brant, D. A.; Goebel, K. D. *Macromolecules* **1972**, *5*, 536.
- (60) Kroon-Batenburg, L. M. J.; Kruiskamp, P. H.; Vliegthart, J. F. G.; Kroon, J. *J. Phys. Chem. B* **1997**, *101*, 8454.
- (61) Kondo, T.; Sawatari, C. *Polymer* **1996**, *37*, 393.
- (62) Kamide, K.; Saito, M. *Polym. J. (Tokyo)* **1985**, *17*, 919.
- (63) Alfthan, E.; De Ruvo, A.; Brown, W. *Polymer* **1973**, *14*, 329.
- (64) Bradley, S. A.; Carr, S. H. *J. Polym. Sci., Polym. Phys. Ed.* **1976**, *14*, 111.
- (65) Salmen, N. L.; Back, E. L. *Tappi* **1977**, *60*, 137.
- (66) Manabe, S.; Iwata, M.; Kamide, K. *Polym. J. (Tokyo)* **1986**, *18*, 1.